A Mode-Switching Based Phase Shift Control for Optimized Efficiency and Wide ZVS Operations in Wireless Power Transfer Systems

Zhu, Gangwei; Dong, Jianning; Shi, Wenli; Soeiro, Thiago Batista; Xu, Junzhong; Bauer, Pavol

DOI
10.1109/TPEL.2022.3231451

Publication date
2022

Document Version
Final published version

Published in
IEEE Transactions on Power Electronics

A Mode-Switching-Based Phase Shift Control for Optimized Efficiency and Wide ZVS Operations in Wireless Power Transfer Systems

Gangwei Zhu, *Student Member, IEEE*, Jianning Dong, *Senior Member, IEEE*, Wenli Shi, *Student Member, IEEE*, Thiago Batista Soeiro, *Senior Member, IEEE*, Junzhong Xu, *Member, IEEE*, and Pavol Bauer, *Senior Member, IEEE*

***Abstract*—This article proposes a mode-switching-based phase shift control (MS-PSC) for wireless power transfer (WPT) systems, which is able to achieve power regulation, load matching, and wide ZVS operations simultaneously without using additional dc–dc converters. Based on the mode transitions between the full-bridge, mixed-bridge, and half-bridge modes of both the inverter and the rectifier, the MS-PSC method guarantees a wide-range ZVS with minimized circulation of reactive power. Therefore, the system efficiency is improved over a wider power range compared to the conventional triple-phase-shift (TPS) control and the existing hybrid modulation control. The principles of different operating modes are analyzed. Then, the implementation of the proposed MS-PSC method and the mode selection strategy are presented. Finally, the effectiveness of the proposed MS-PSC method is validated in a WPT prototype. Experimental results show that the proposed MS-PSC method can achieve a high overall efficiency in a wide power range. Compared with the conventional TPS control, the MS-PSC method further optimizes the efficiency in 10%–63% of the rated power, with efficiency improvements ranging from 1.5% to 6%. As a result, the system efficiency remains at 93.5%–96.1% in the power range of 1–10 kW, with the transformer coupling coefficient k = 0.19.**

***Index Terms*—Load matching, mode switching, power regulation, wireless power transfer (WPT), zero-voltage-switching (ZVS).**

I. Introduction

WIRELESS power transfer (WPT) enables safe, convenient, and automated charging for electric vehicles (EVs) [1], [2], [3], [4], [5], [6], [7], [8]. For wireless charging of EVs, batteries act as the loads of the WPT systems. Due to the noticeable variation of battery profiles during the charging process, it is vital for WPT systems to achieve accurate power flow control over a wide operating range [3]. Generally, there are three important objectives to design a controller for WPT systems. First, it is necessary for the controller to provide the desired output based on the load profiles. For EV battery charging, the process is typically divided into two stages: constant current (CC) and constant voltage (CV). Therefore, CC/CV output is the fundamental control target of the WPT systems designed for EVs. Second, in order to improve transmission efficiency as well as to reduce electromagnetic interference (EMI) of the system, the implementation of zero-voltage-switching (ZVS) operations across the semiconductors of the typically used resonant converter serve as another important consideration for the controller design [9]. Third, to realize the optimized efficiency, the optimal load tracking has become an increasingly important performance indicator in the WPT systems [10], [11]. Thus, it is desired to realize load matching.

Over the past decades, numerous studies have been carried out to meet the abovementioned control objectives, which can be roughly divided into three groups: 1) using dc–dc converters [12], [13]; 2) phase shift control [14], [15], [16], [17], [18], [19], [20]; 3) pulse density modulation and ON–OFF keying modulation [21], [22].

In order to realize power regulation and load matching simultaneously, a commonly used approach is to cascade dc/dc converters in the front- and/or back-end of the WPT systems [12], [13]. Dai et al. [12] proposed a maximum efficiency tracking method with two dc–dc converters installed in the front- and back-end of the system, respectively. In this method, a primary-side dc–dc converter is used to provide a stable load voltage, while a secondary-side dc–dc converter is employed for maximum efficiency tracking. Huang et al. [13] proposed a control technique based on the perturbation and observation (P&O). The load-side dc–dc converter is responsible for output regulation, while the front-side converter is used to minimize the input power through P&O methods. Although dc–dc converters can realize the control objectives, it also brings extra losses, increased costs, and reduced power density.

Manuscript received 28 June 2022; revised 2 November 2022; accepted 15 December 2022. Date of publication 23 December 2022; date of current version 14 February 2023. The work was supported by China Scholarship Council under Grant 202106230112. The work of Gangwei Zhu was supported by CSC. Recommended for publication by Associate Editor K. Ngo. *(Corresponding author: Jianning Dong.)*

Gangwei Zhu, Jianning Dong, Wenli Shi, and Pavol Bauer are with the DC System, Energy Conversion and Storage Group, Faculty of Electrical Engineering, Mathematics and Computer Science, Delft University of Technology, 2624 Delft, The Netherlands (e-mail: g.zhu-2@tudelft.nl; j.dong-4@tudelft.nl; w.shi-3@tudelft.nl; p.bauer@tudelft.nl).

Thiago Batista Soeiro is with the Faculty of Electrical Engineering, Mathematics and Computer Science, University of Twente, 7522 Enschede, The Netherlands (e-mail: t.batistasoeiro@utwente.nl).

Junzhong Xu is with the Faculty of Electrical Engineering, Shanghai Jiao Tong University, Shanghai 200240, China (e-mail: junzhongxu@sjtu.edu.cn).

Color versions of one or more figures in this article are available at https://doi.org/10.1109/TPEL.2022.3231451.

Digital Object Identifier 10.1109/TPEL.2022.3231451

Another typical method for power regulation is phase shift control. In [14], phase shift control was implemented in the primary-side inverter for load matching. In this method, the front-end dc–dc converter is avoided by introducing an active control of the inverter. However, the load-side dc–dc converter is still needed to achieve the desired output control metrics, which results in extra power losses and costs. In order to further eliminate the load-side dc–dc converter, an active rectifier can be utilized to regulate the equivalent load impedance [15], [16]. Based on the active rectifier, a dual-phase-shift (DPS) control method was proposed in [17], where the phase shift angles of the inverter and rectifier stages were adjusted cooperatively to achieve power regulation and load matching simultaneously. Nevertheless, the phase difference between the ac port voltages of the inverter and rectifier is maintained at 90° in this method, resulting in hard switching of some power switches. In order to realize wide ZVS operations, a triple-phase-shift (TPS) control method was proposed in [18], where the phase difference of the dual-side ac voltages was served as a new control variable to realize ZVS under a wide output power. However, this approach introduces large reactive power in the resonant tank. This means that higher coil currents are needed to deliver the same amount of power, which increases the power losses of the system. Moreover, some researchers have introduced new control variables to achieve the optimal control of the WPT systems. Wang et al. [19] proposed a switch-controlled capacitor-based phase shift modulation (SCC-PSM) to provide the desired output and realize wide ZVS operations. However, the use of SCC leads to additional power losses. In order to avoid additional components, Hu et al. [20] proposed a variable frequency phase shift control (VFPSC) to realize ZVS operations under wide load variations. Nevertheless, in this method, the switching frequency needs to be regulated far away from the resonant frequency to ensure wide ZVS operations. This makes the system highly detuned, resulting in a reduced overall efficiency.

Apart from phase shift control, pulse density modulation [21] and ON–OFF keying modulation [22] were recently developed to facilitate ZVS. Since the pulsewidth of the inverter output voltage is constant in these methods, ZVS operations can be easily implemented with minimal reactive power. However, considerable output voltage ripple deteriorates the performance of these methods under light load conditions due to the missing pulses in [21] and the "OFF" state in [22].

Recently, some researchers combined the half-bridge (HB) mode and the full-bridge (FB) mode to improve the system efficiency under light load conditions. Li et al. [23] proposed a hybrid modulation control (HMC) method to improve the light-load efficiency, where both the inverter and rectifier can operate in the FB and HB modes based on the output power. Compared to the conventional TPS method, the HMC method achieves further efficiency optimization in 16.7%–40% of the rated power. However, due to the limited power transfer capability of the HB mode, the converters still operate in the FB mode at most power levels and the efficiency optimization range is narrow. Wu et al. [24] proposed a dual-sided control strategy based on mode switching (DSC-MS), where the mixed-bridge (MB) mode was utilized to widen the operating range of the inverter. For the MB mode, the inverter operates in the FB and HB modes alternatively in each two switching cycles, which extends the regulation range of the inverter output voltage. In the DSC-MS method, load matching is realized through mode switching of the inverter, while output regulation is achieved by the phase shift control of a semiactive rectifier. Nevertheless, phase shift control of the inverter is missing in this method, and therefore, wide power regulation still relies on the voltage control of the front-stage power factor correction (PFC) converter. Besides, since the MB and HB modes are not considered in the rectifier control, the efficiency under light load conditions is still low. In [24], the system efficiency was only 88.7% at 14.8% of the rated power.

To fill up the research gaps mentioned above, this article proposes a mode-switching-based phase shift control (MS-PSC) for WPT systems. In this method, an active rectifier is adopted and hybrid modes of both the inverter and rectifier are considered. Both the inverter and rectifier can switch in FB, MB, and HB modes to provide the desired output and achieve load matching. ZVS operations of all power switches are realized under a wide range of power levels. To sum up, the main contributions of this article are listed as follows.

1) Wide power regulation in 10%–100% of the rated power is achieved without using additional dc–dc converters.
2) Thanks to the effective use of the FB, MB, and HB modes and the joint control of the inverter and rectifier, wide ZVS operations are realized with minimized circulation of reactive power. Therefore, an overall efficiency of 93.5%–96.1% is obtained within 10%–100% of the rated power. Compared with the conventional TPS control, the MS-PSC method further optimizes the efficiency in 10%–63% of the rated power, with efficiency improvements ranging from 1.5% to 6%.
3) A mode selection strategy is proposed, which enables the WPT system to switch automatically to the optimal operating mode based on the required output features.
4) A harmonic-considered model is adopted to evaluate the influence of harmonics in the MB and HB modes.

The rest of this article is organised as follows. Section II demonstrates the fundamental characteristic of the series–series (SS) compensated WPT system. Besides, the conventional phase shift control method is briefly reviewed in this section. In Section III, the working principles of the MB and HB modes are presented, and the mode selection strategy as well as the control scheme of the proposed MS-PSC are introduced. In Section IV, experimental results are given to verify the effectiveness of the MS-PSC method. Finally, Section V concludes this article.

II. Review of the SS-Compensated WPT System Using Phase Shift Control

A. Equivalent Circuit Model

Fig. 1 shows the circuit diagram of a typical SS compensated WPT system with an active rectifier. In Fig. 1, U_{in} and U_{out} are the dc input and output voltages, respectively; I_{out} is the dc output current; v_{ab} is the inverter output voltage and v_{cd} is the rectifier input voltage; i_P and i_S represent the primary and secondary coil currents. Moreover, L_P, C_P, L_S, and C_S

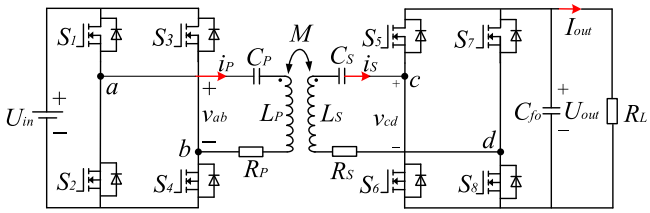

Fig. 1. Circuit diagram of the SS-compensated WPT system with an active rectifier stage.

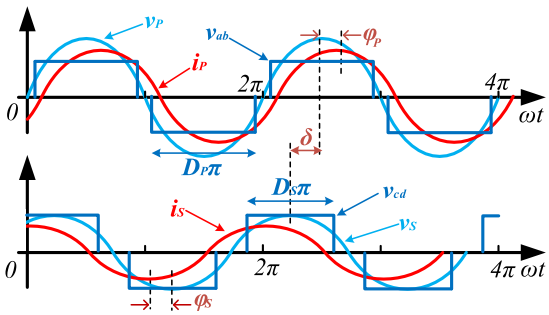

Fig. 2. Typical waveforms of the WPT system using phase shift control. Herein, it can be observed that ZVS operations are realized in both the inverter and rectifier stages.

are the self-inductances and compensation capacitors of the transmitter coil and the receiver coil, respectively; M is the mutual inductance between the transmitter and receiver coils; R_P and R_S represent the equivalent loss resistances of the coils and compensation capacitors in the primary and secondary sides; R_L is the equivalent resistive modeling of the load.

To provide the desired output power, phase shift control is typically adopted. The operation waveforms of the WPT system using phase shift control are shown in Fig. 2. Herein, D_P and D_S ($0 < D_P \leq 1, 0 < D_S \leq 1$) are the duty cycles of v_{ab} and v_{cd}, which can be adjusted by changing the phase shift angles of the inverter and rectifier. δ is defined as the phase difference between v_P and v_S, where v_P and v_S are the fundamental component of v_{ab} and v_{cd}, respectively. Moreover, the phase difference between v_P and i_P is denoted by φ_P, and the phase difference between v_S and i_S is represented by φ_S. For the SS-compensated WPT system, the compensation capacitors C_P and C_S are designed to be resonant with the coil inductances L_P and L_S at the resonant frequency f_s, i.e.,

$$\omega_s = \frac{1}{\sqrt{L_P C_P}} = \frac{1}{\sqrt{L_S C_S}} \tag{1}$$

where $\omega_s = 2\pi f_s$ is the resonant angular frequency. Due to the bandpass filtering characteristic of the SS-compensated resonant network, the high-order harmonics of the coil currents are negligible. Therefore, the fundamental frequency approximation method is typically adopted for simplification [15]. According to the analysis in [15], the steady-state equation of the system can be simplified as

$$\begin{cases} \dot{V}_P & \approx -j\omega M \dot{I}_S \\ \dot{V}_S & \approx j\omega M \dot{I}_P \end{cases} \tag{2}$$

where $\dot{V}_P$, $\dot{V}_S$, $\dot{I}_P$, $\dot{I}_S$ are the phasors of v_P, v_S, i_P, i_S, respectively; M can be expressed as $M = k\sqrt{L_P L_S}$, with k representing the coupling coefficient of the coils. Furthermore, the phase difference φ_P between $\dot{V}_P$ and $\dot{I}_P$, as well as the phase difference φ_S between $\dot{V}_S$ and $\dot{I}_S$ are given by

$$\begin{cases} \varphi_P = & \pi/2 - \delta \\ \varphi_S = & \pi/2 - \delta. \end{cases} \tag{3}$$

Based on the Fourier series expansion, the phasor forms of the ac voltages on both sides are obtained as

$$\begin{cases} \dot{V}_P = & K_P U_{in} \sin[(D_P\pi)/2] \angle 0 \\ \dot{V}_S = & K_S U_{out} \sin[(D_S\pi)/2] \angle \delta \end{cases} \tag{4}$$

where K_P and K_S denote the dc to ac voltage gains of the inverter and rectifier, respectively. Typically, both the inverter and rectifier operate in the FB mode, and the voltage gain K_P and K_S can be deduced as

$$\begin{cases} K_{P\_FB} = & 2\sqrt{2}/\pi \\ K_{S\_FB} = & 2\sqrt{2}/\pi. \end{cases} \tag{5}$$

The subscript FB indicates that the converter operates in the FB mode. Furthermore, substituting (4) into (2), the amount of output active power P_{out} and circulating reactive power Q_{cir} of the system can be obtained as

$$P_{out} = \mathrm{Re}\{\dot{V}_S \dot{I}_S^*\} = \frac{|\dot{V}_P||\dot{V}_S|\sin(\delta)}{\omega M} \tag{6}$$

$$Q_{cir} = \mathrm{Im}\{\dot{V}_S \dot{I}_S^*\} = -\frac{|\dot{V}_P||\dot{V}_S|\cos(\delta)}{\omega M}. \tag{7}$$

As it can be seen from (6), the direction of the transferred active power P_{out} is determined by the phase angle δ. The active power flows from the primary side to the secondary side when $0 < \delta < \pi$, while the transfer direction is reversed when $-\pi < \delta < 0$. This article only consider the case where the power flows from the primary side to the secondary side, and the phase angle δ should satisfy $0 < \delta < \pi$. In fact, the control strategy for the reverse power flow can be obtained by setting δ to be a negative value and repeating the analysis described in the following section. Due to the space limitations, the analysis for reverse power flow will not be described. For the forward power flow, as shown in (6) and (7), the amount of output power P_{out} is maximized at $\delta = \pi/2$, with the reactive power Q_{cir} minimized simultaneously. Therefore, it is desired to let the system work in $\delta = \pi/2$ to enhance its power transfer capability as well as to minimize the circulating reactive power in the resonant tank.

B. Maximum Efficiency of the Resonant Tank

In this section, the power losses of the resonant tank are analyzed to obtain the maximum efficiency point. According to the analysis in [18], the transfer efficiency of the resonant tank is obtained as

$$\eta = \frac{\omega M \sin(\delta)}{R_P T + R_S/T + \omega M \sin(\delta)} \tag{8}$$

TABLE I
SYSTEM PARAMETERS OF THE SS-COMPENSATED WPT SYSTEM

Symbol	Parameters	Value	Unit
M	Mutual inductance	46	μH
L_P	Primary coil inductance	293.8	μH
L_S	Secondary coil inductance	198.8	μH
C_P	Primary compensation capacitor	12.0	nF
C_S	Secondary compensation capacitor	17.6	nF
R_P	Primary loss resistance	0.21	Ω
R_S	Secondary loss resistance	0.14	Ω
U_{in}	DC input voltage	600	V
U_{out}	DC output voltage	400∼600	V
f_s	Switching frequency	85	kHz
δ_m	Margin angle	16	°

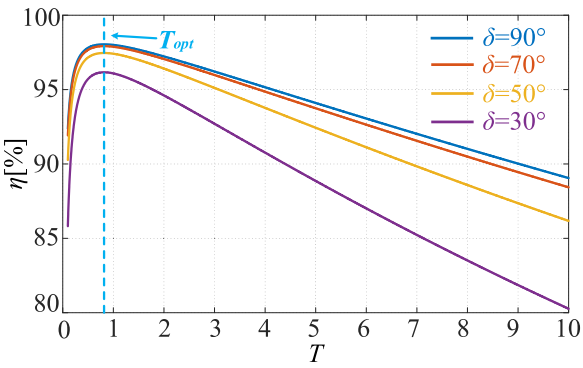

Fig. 3. Resonant tank transfer efficiency η with different values of ac voltage ratio T and phase shift angle δ.

where T is the ratio of the ac voltages on the primary and secondary sides, which is expressed as

$$T = \frac{|\dot{V}_S|}{|\dot{V}_P|} = \frac{K_S U_{out} \sin[(D_P\pi)/2]}{K_P U_{in} \sin[(D_P\pi)/2]}. \tag{9}$$

As it can be seen from (8), η varies with the ac voltage ratio T and the phase shift angle δ. With the parameters listed in Table I, η as a function of different values of T and δ is shown in Fig. 3. According to Fig. 3, the maximum efficiency is achieved under a certain voltage ratio T. The optimal voltage ratio T_{opt} can be deduced by solving the derivative of η with respect to T, i.e.,

$$\frac{d\eta}{dT} = 0 \Rightarrow T_{opt} = \sqrt{\frac{R_S}{R_P}}. \tag{10}$$

As illustrated in Fig. 3, the maximum efficiency of the resonant tank is always obtained at T_{opt} regardless of the variation of δ. It should be noted that the concept of optimal voltage ratio is equivalent to the concept of load matching [18]. Apart from the voltage ratio T, another factor that affects η is the phase angle δ. As shown in Fig. 3, when δ deviates from 90°, η decreases accordingly. Therefore, in order to achieve a higher efficiency, the deviation of δ from 90° should be minimized.

C. Implementation of ZVS

For the WPT system operating at a high switching frequency, ZVS operations of the power switches are of great importance. In this article, MOSFETs are used as the switches of the converters. To realize the ZVS of the inverter working in the FB mode, the antiparallel diode of the MOSFET should conduct before the turn-ON instant. This implies that the current i_P should lag the voltage v_P, as shown in Fig. 2. Specifically, the duty cycle D_P and the phase angle φ_P should satisfy

$$\varphi_P \geq \frac{(1 - D_P)\pi}{2}. \tag{11}$$

Similarly, for ZVS operations of the rectifier operating in the FB mode, D_S and φ_S should satisfy

$$\varphi_S \geq \frac{(1 - D_S)\pi}{2}. \tag{12}$$

D. Conventional Triple Phase Shift Control

In order to achieve wide ZVS operations for all power switches, a TPS control method was proposed in [18]. In this method, the phase angle δ serves as a new control variable to adjust the phase angles φ_P and φ_S for wide ZVS operations. Substituting (11) and (12) into (3), the ZVS condition for all power switches is obtained as

$$\begin{cases} \delta \leq (D_P\pi)/2 \\ \delta \leq (D_S\pi)/2. \end{cases} \tag{13}$$

To reduce the reactive power in the resonant tank, δ should be as close to 90° as possible, and therefore, δ is selected by

$$\delta = \min\{(D_P\pi)/2, (D_S\pi)/2\} - \delta_m. \tag{14}$$

where δ_m is the margin angle to ensure the turn-ON current is large enough to charge/discharge the equivalent output capacitor C_{oss} of the power switches within the set dead time [21]. Although the TPS control is able to realize wide ZVS operations, one problem is that as the desired output power drops, the duty cycles D_P and D_S decrease accordingly, and therefore, the value of δ should be lowered to ensure ZVS operations. This means that a small value of δ is needed when the output power deviates far away from the rated power. However, according to (7), a small value of δ leads to a large amount of reactive power. Therefore, in order to maintain a high overall efficiency, a larger phase angle δ is desired.

III. PROPOSED MODE SWITCHING-BASED PHASE SHIFT CONTROL

According to the analysis in Section II-D, the TPS control suffers from the problem of large reactive power under light load conditions. However, if the deviation of δ from 90° can be minimized, the reactive power can be reduced and a higher transfer efficiency can be obtained. In this section, the proposed MS-PSC method is demonstrated, where power regulation, wide ZVS operations, and load matching are realized simultaneously. Besides, this method enables the inverter and rectifier to operate in FB, MB, and HB modes, and thus, the deviation of δ from 90° is minimized.

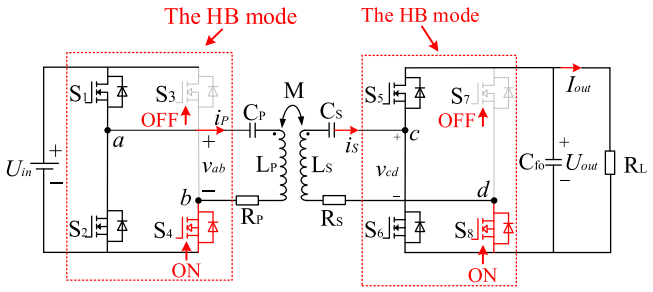

Fig. 4. Circuit diagram of the WPT system with the inverter and rectifier working in the HB mode.

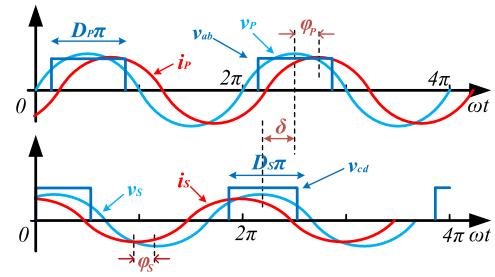

Fig. 5. Operating waveforms of the inverter and rectifier working in the HB mode.

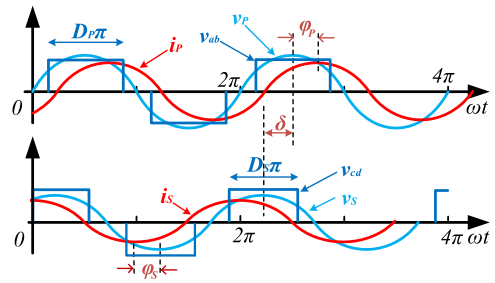

Fig. 6. Operating waveforms of the inverter and rectifier working in the MB mode.

A. Analysis of Different Operating Modes

Substituting (4) into (6), the output power of the system is expressed by

$$P_{out} = \frac{U_{in}U_{out}K_PK_S\sin[(D_P\pi)/2]\sin[(D_S\pi)/2]\sin(\delta)}{\omega M}. \tag{15}$$

As illustrated in (15), the output power of the system can be regulated by various parameters. However, for a typical WPT system, the dc input voltage U_{in}, the operating angular frequency ω, as well as the mutual inductance M are almost constant during operation. The dc output voltage U_{out} depends on the load profiles, e.g., the battery voltage. Therefore, power regulation is typically achieved by adjusting the duty cycles D_P and D_S. As the desired output power P_{out} drops, D_P and D_S should be decreased accordingly. This means that a smaller δ is needed for ZVS. Nevertheless, further observation of (15) reveals that the values of K_P and K_S also affect the amount of transferred power, which can be adjusted by switching the working modes of the inverter and rectifier. Thus, lowering K_P and K_S through mode switching can be a feasible way to reduce the drop of D_P and D_S under light- and medium-power levels, which narrows the deviation of δ from 90°.

Based on the HMC method proposed in [23], the converters on both sides can operate in the FB and HB modes. The operating principle of the FB mode was already discussed in Section II and will not be repeated in this section. For the HB mode, as shown in Fig. 4, when the power switch S_3 keeps an "OFF" state while S_4 maintains an "ON" state during the whole operation, the inverter operates in the HB mode. Similarly, when the power switch S_7 keeps an "OFF" state while S_8 maintains an "ON" state all the time, the rectifier operates in the HB mode. The operating waveforms of the WPT system with both the inverter and rectifier working in the HB mode is shown in Fig. 5. According to the Fourier series expansion, the fundamental components of the ac voltages $\dot{V}_P$ and $\dot{V}_S$ in the HB mode are derived by

$$\begin{cases} \dot{V}_P = & K_{P\_HB}U_{in}\sin[(D_P\pi)/2]\angle 0 \\ \dot{V}_S = & K_{S\_HB}U_{out}\sin[(D_S\pi)/2]\angle\delta \end{cases} \tag{16}$$

where

$$\begin{cases} K_{P\_HB} = & \sqrt{2}/\pi \\ K_{S\_HB} = & \sqrt{2}/\pi. \end{cases} \tag{17}$$

Apart from the FB and HB modes, the MB mode is employed in this article, where the converter operates alternately in the FB mode and the HB mode. The working waveforms of the system with both the inverter and rectifier operating in the MB mode are depicted in Fig. 6. As it can be seen from Fig. 6, in each two switching cycles, the converters operate in the FB mode in one switching cycle, and then switch to the HB mode in the other switching cycle. Based on the Fourier series expansion, the fundamental components of $\dot{V}_P$ and $\dot{V}_S$ in the MB mode are derived by

$$\begin{cases} \dot{V}_P = & K_{P\_MB}U_{in}\sin[(D_P\pi)/2]\angle 0 \\ \dot{V}_S = & K_{S\_MB}U_{out}\sin[(D_S\pi)/2]\angle\delta \end{cases} \tag{18}$$

where

$$\begin{cases} K_{P\_MB} = & 3\sqrt{2}/2\pi \\ K_{S\_MB} = & 3\sqrt{2}/2\pi. \end{cases} \tag{19}$$

For ZVS operations in the HB and MB modes, as it can be observed in Figs. 5 and 6, the inverter current i_P should lag the inverter voltage v_P at least by $[(1-D_P)\pi/2]$, while the rectifier current i_S should lead the rectifier voltage v_S at least by $[(1-D_S)\pi/2]$. It should be noted that ZVS constraints in the HB and MB modes are consistent with the FB mode. Therefore, (11) and (12) are still applicable for analyzing ZVS in the HB and MB modes.

On the other hand, as it can be seen from (5), (17), and (19), the voltage gains K_P and K_S decrease accordingly as the converter mode switches from the FB mode to the MB mode and then to the HB mode, i.e., from $2\sqrt{2}/\pi$ to $3\sqrt{2}/2\pi$ and then to $\sqrt{2}/\pi$. This implies that as the output power P_{out} decreases, the converters can switch from the FB mode to the HB mode or the

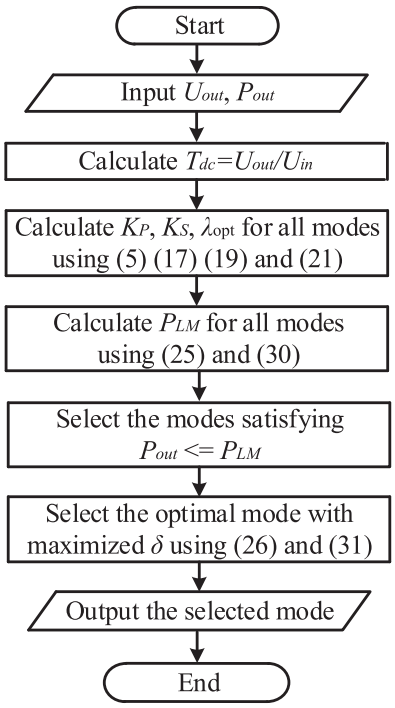

Fig. 7. Flowchart of the proposed mode selection strategy.

MB mode to narrow the variation of duty cycles D_P and D_S, and thus, a smaller deviation of δ from 90° can be obtained. In this article, the proposed MS-PSC method allows both the inverter and rectifier to switch between the above three operating modes, thereby reducing the deviation of δ from 90°. Compared with the conventional TPS control, the proposed MS-PSC method reduces the reactive power at light- and medium-power levels, and the system efficiency is therefore maintained high in a wide power range.

B. Mode Selection

According to the analysis in the previous section, it is preferable to consider the HB and MB modes to reduce the reactive power under light- and medium-load conditions. Nevertheless, the power transfer capability of the system varies as the converters switch between different modes. Therefore, it is of great importance to select an ideal operating mode based on the required output power. In this article, a mode selection strategy is proposed, where the optimal mode of the system is selected with both load matching and ZVS operations taken into consideration. The flowchart of the proposed mode selection strategy is shown in Fig. 7.

As discussed in Section II-B, in order to realize load matching, an optimal ac voltage ratio T_{opt} is needed as follows:

$$T_{opt} = \frac{K_S U_{out} \sin[(D_S\pi)/2]}{K_P U_{in} \sin[(D_P\pi)/2]} = \sqrt{\frac{R_S}{R_P}}. \tag{20}$$

As it can be observed from (20), there is an optimal ratio between the duty cycles D_P and D_S when load matching is realized. In order to demonstrate the ratio between D_P and D_S, the factor λ is introduced and defined as $\lambda = \sin[(D_S\pi)/2]/\sin[(D_P\pi)/2]$. According to (20), the optimal ratio between D_P and D_S under load matching is given by

$$\lambda_{opt} = \frac{\sin[(D_S\pi)/2]}{\sin[(D_P\pi)/2]} = \frac{K_P}{K_S T_{dc}} \sqrt{\frac{R_S}{R_P}} \tag{21}$$

where T_{dc} is the ratio between the dc input voltage U_{in} and the dc output voltage U_{out}, i.e., $T_{dc} = U_{out}/U_{in}$. As illustrated in (21), the value of λ_{opt} depends on the voltage gains K_P and K_S. Therefore, λ_{opt} varies as the system switches between different operating modes. Besides, the value of λ_{opt} affects the power transfer capability of the system. Based on the value of λ_{opt}, there are two cases that should be considered.

Case I: $\lambda_{opt} >= 1$

In this case, the optimal ratio between D_P and D_S under load matching is given by

$$\lambda_{opt} = \frac{\sin[(D_S\pi)/2]}{\sin[(D_P\pi)/2]} \geq 1 \Rightarrow D_P \leq D_S. \tag{22}$$

As it can be observed from (22), D_S is larger than D_P in this case. According to the ZVS constraints described in (14), the phase difference δ for ZVS is selected by

$$\delta = (D_P\pi)/2 - \delta_m. \tag{23}$$

Substituting (21) and (23) into (15), the output power expression in this case is given by (24) which is shown at the top of the next page. As can be observed in (24), the output power P_{out} is a monotonic increasing function of the duty cycle D_S. Considering the upper limit of D_S, the power transfer capability under load matching is obtained as

$$\begin{aligned} P_{out} &= \frac{U_{in}^2 T_{dc} K_P K_S \sin^2[(D_S\pi)/2]}{\lambda_{opt}\omega M} \left\{ \frac{\sin[(D_S\pi)/2]}{\lambda_{opt}} \cos(\delta_m) \right. \\ &\quad \left. - \sqrt{1 - \frac{\sin^2[(D_S\pi)/2]}{\lambda_{opt}^2}} \sin(\delta_m) \right\}. \end{aligned} \tag{24}$$

$$P_{LM} = \frac{U_{in}^2 T_{dc} K_P K_S [\cos(\delta_m) - \sqrt{\lambda_{opt}^2 - 1} \sin(\delta_m)]}{\lambda_{opt}^2 \omega M}. \tag{25}$$

As it can be observed in (25), the power transfer capability P_{LM} depends on the voltage gains K_P and K_S, which are determined by the working mode of the inverter and rectifier. In other words, P_{LM} can be calculated once the operating mode is selected. For a selected mode, if the required output power P_{out} satisfies $P_{out} \leq P_{LM}$, it indicates that the power transfer capability of the system is able to meet the load demand. However, there might be several operating modes that can satisfy the load requirement at the same time. Thus, it is necessary to find an optimal mode among all the eligible modes. According to the analysis in Section II-D, the phase difference δ should be as large as possible to minimize the reactive power in the resonant tank. Therefore, the operating mode with maximized δ should be selected. Substituting (21)

and (23) into (15), the value of δ should satisfy

$$\sin^2(\delta+\delta_m)\sin(\delta)=\frac{\omega M P_{out}}{\lambda_{opt}U_{in}^2 T_{dc}K_P K_S}. \tag{26}$$

With given P_{out} and U_{out}, the optimal mode with maximized δ can be selected by solving (26).

Case II: $\lambda_{opt}<1$

In this case, the optimal ratio between D_P and D_S under load matching can be expressed as

$$\lambda_{opt}=\frac{\sin[(D_S\pi)/2]}{\sin[(D_P\pi)/2]}<1\Rightarrow D_P>D_S. \tag{27}$$

According to (27), D_P is larger than D_S, and the phase angle δ for ZVS is selected by

$$\delta=(D_S\pi)/2-\delta_m. \tag{28}$$

Then, substituting (21) and (28) into (15), the output power expression of the system is given by (29) which is shown at the top of next page. Considering the upper limit of the duty cycle D_P, the power transfer capability with the load matching is derived by

$$\begin{aligned}P_{out}=&\frac{U_{in}^2 T_{dc}K_P K_S\lambda_{opt}\sin^2[(D_P\pi)/2]}{\omega M}\\&\times\{\lambda_{opt}\sin[(D_P\pi)/2]\cos(\delta_m)\\&-\sqrt{1-\lambda_{opt}^2\sin^2[(D_P\pi)/2]}\sin(\delta_m)\Big\}.\end{aligned} \tag{29}$$

$$P_{LM}=\frac{U_{in}^2 T_{dc}K_P K_S[\lambda_{opt}\cos(\delta_m)-\sqrt{1-\lambda_{opt}^2}\sin(\delta_m)]}{\omega M}. \tag{30}$$

Similarly, substituting (21), (28) into (15), δ should satisfy

$$\sin^2(\delta+\delta_m)\sin(\delta)=\frac{\lambda_{opt}\omega M P_{out}}{U_{in}^2 T_{dc}K_P K_S}. \tag{31}$$

According to (31), the optimal mode with maximized δ can be selected in the case of $\lambda_{opt}<1$.

With the parameters listed in Table I, the selected optimal mode against the desired output power P_{out} and the dc output voltage U_{out} is shown in Fig. 8. It should be noted that "FB-MB" in Fig. 8 means that the inverter operates in the FB mode, while the rectifier works in the MB mode. As illustrated in Fig. 8, when the desired output power P_{out} decreases, the converters switch from the FB mode to the MB mode and the HB mode, which narrows the deviation of δ from 90° and reduces the reactive power under light- and medium- loads. Although the "FB-HB" mode and the "HB-FB" mode can be selected based on the HMC method, these two modes are not the optimal mode when the MB mode is considered. Therefore, the "FB-HB" mode and "HB-FB" mode are not selected in this article. Besides, the load matching boundary is also depicted in Fig. 8. When the desired output power P_{out} exceeds this boundary, load matching is sacrificed for power tracking capability, and D_P or D_S is regulated to the full duty cycle.

In order to demonstrate the improvement in the value of δ, δ versus P_{out} is plotted in Fig. 9, when considering the parameters

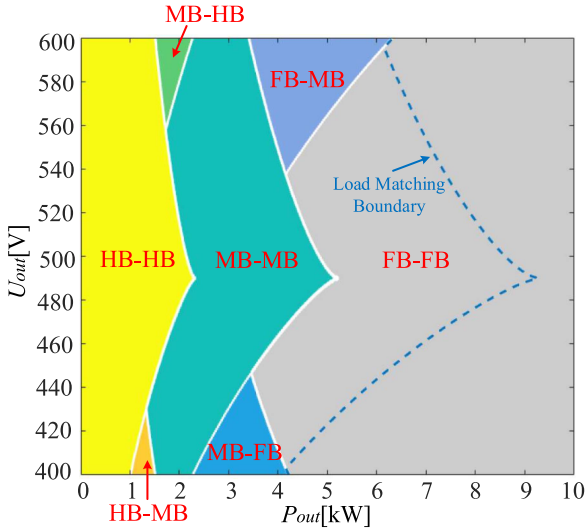

Fig. 8. Optimal operating mode of the WPT system based on the proposed mode selection strategy.

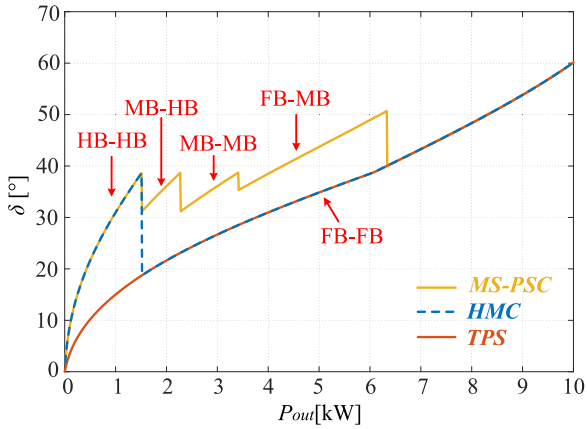

Fig. 9. Phase difference δ versus the desired output power P_{out}.

listed in Table I and the output voltage U_{out} controlled to 600 V. In Fig. 9, the results of the conventional TPS method, the HMC method, and the MS-PSC method are benchmarked. Compared with the TPS method, as it can be seen in Fig. 9, the value of δ in the MS-PSC method is improved significantly in the power range of 0–6.3 kW. For the HMC method, although this method can enhance the value of δ under light load conditions, i.e., 0-1.6 kW, the optimization range is narrow due to the limited power transfer capability of the HB mode. With a larger δ obtained in the MS-PSC method, the reactive power in the resonant tank is reduced remarkably and a higher overall efficiency can be achieved.

C. Mode Switching-Based Control Scheme

The block diagram of the proposed MS-PSC method is shown in Fig. 10. Generally, the controller of the WPT system is designed for constant voltage (CV) or constant current (CC) output. For the SS-compensated WPT system, the CC output can

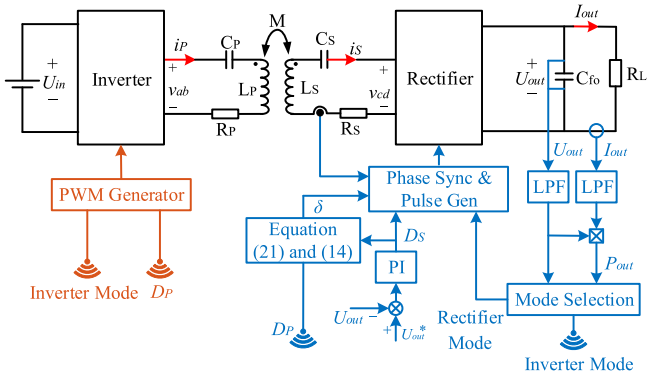

Fig. 10. Block diagram of the proposed MS-PSC method.

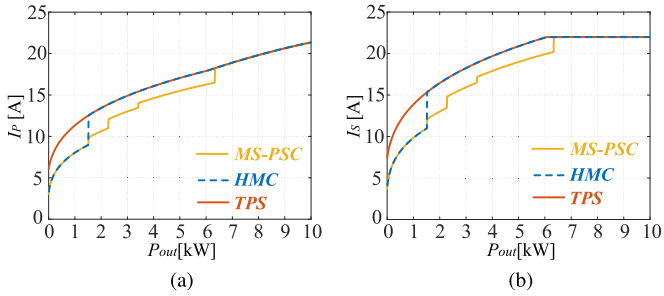

Fig. 11. RMS values of coil currents versus the desired output power P_{out}. (a) Primary coil current I_P. (b) Secondary coil current I_S.

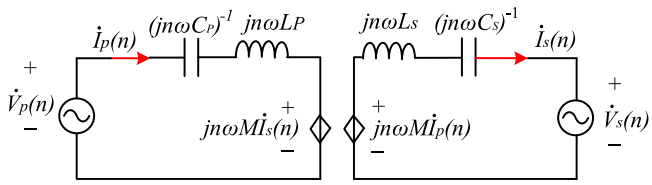

Fig. 12. Harmonic-considered circuit model of the SS-compensated WPT system.

be realized by reasonable parameter design without regulating control variables. Therefore, CV output is the control objective in this article. In the MS-PSC method, the duty cycle D_S is controlled to realize a constant output voltage. Besides, the duty cycle D_P is regulated to realize load matching, whilst δ is adjusted to achieve wide ZVS range.

As illustrated in Fig. 10, the dc output voltage U_{out} and current I_{out} are sampled. Two separate low-pass-filters (LPFs) are utilized to filter the ripple of U_{out} and I_{out}. Then, the filtered U_{out} and I_{out} are multiplied to obtain the output power P_{out}. The measured output power P_{out}, combined with the filtered U_{out}, are fed to the mode selection module. The operating modes of the inverter and rectifier are then determined based on the proposed mode selection strategy. A PI controller is adopted to regulate the duty cycle D_S for a constant output voltage. The duty cycle D_P and the phase difference δ are calculated after the value of D_S is determined. When the output power P_{out} is lower than the load-matching boundary, the relationship between D_P and D_S should always satisfy (21). If P_{out} exceeds the load matching boundary, load matching is sacrificed, and D_P or D_S is regulated to the full duty cycle. To ensure wide ZVS, δ should be selected by (14) at all power points. It should be noted that a hysteresis comparator is needed in the mode selection module to avoid switching back and forth when the output power is at the power boundary between two different modes.

D. Reduction of Coil Currents and Overall Power Losses

The overall power losses of the WPT system mainly include the power losses of the resonant tank and the power losses of the converters. According to the analysis in [25], the power losses of each part are related to the rms values of coil currents. With the parameters listed in Table I and $U_{out} = 600\,V$, the rms values of coil currents I_P and I_S versus the output power P_{out} are plotted in Fig. 11, where the results of the TPS method, the HMC method and the proposed MS-PSC method are compared. As it can be seen, when delivering the same amount of power, I_P and I_S are reduced in the MS-PSC method. This is because compared with TPS and HMC, the reactive power of the MS-PSC is minimized through mode switching, and thus, smaller coil currents can be obtained. With reduced coil currents in the MS-PSC method, the overall power losses of the system are decreased, and higher transmission efficiency can be achieved. Moreover, compared with the FB mode, the switching losses of the MOSFETs are smaller in the MB and HB modes since the equivalent switching times of the MOSFETs are reduced in the MB and HB modes. Thus, the overall power losses of the system can be further reduced in the MS-PSC method.

E. Influence of Harmonics

It should be noted that in the MB and HB modes, the ac port voltages of the converters contain more harmonics than the FB mode. Therefore, it is essential to take the harmonic components into consideration, which affect ZVS implementation and transfer efficiency. As shown in Fig. 12, a harmonic-considered circuit model is established to evaluate the influence of harmonics, where $\dot{V}_P(n)$ and $\dot{V}_S(n)$ represent the nth-order harmonic components of v_{ab} and v_{cd}; $\dot{I}_P(n)$ and $\dot{I}_S(n)$ represent the nth-order harmonic components of i_P and i_S, respectively. For simplification, R_P and R_S are neglected in this model. For the inverter operating in the MB mode, the time-domain expression of the ac voltage $v_{ab}(t)$ is derived by

$$v_{ab}(t) = \begin{array}{l} \frac{D_P U_{in}}{4} + \frac{2U_{in}}{\pi}\sin(\frac{D_P\pi}{4})\sin(\frac{1}{2}\omega t + \frac{3}{4}\pi) \\ +\frac{3U_{in}}{\pi}\sin(\frac{D_P\pi}{2})\sin(\omega t) + \cdots \end{array}. \tag{32}$$

Similarly, the ac voltage $v_{cd}(t)$ of the rectifier working in the MB mode is obtained as

$$v_{cd}(t) = \begin{array}{l} \frac{D_S U_{out}}{4} + \frac{2U_{out}}{\pi}\sin(\frac{D_S\pi}{4})\sin[\frac{1}{2}(\omega t + \delta) + \frac{3}{4}\pi] \\ +\frac{3U_{out}}{\pi}\sin(\frac{D_S\pi}{2})\sin(\omega t + \delta) + \cdots \end{array}. \tag{33}$$

For the nth-order harmonic components, considering $\dot{V}_P(n)$ and $\dot{V}_S(n)$ as two independent excitation voltage sources and using the superposition theorem, the phasor-domain expression

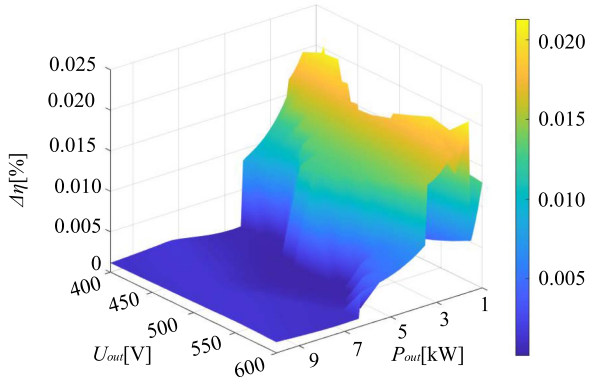

Fig. 13. $\Delta\eta$ against the output voltage U_{out} and the output power P_{out}.

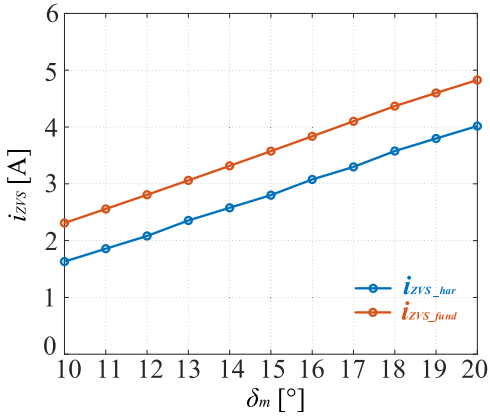

Fig. 14. Minimum ZVS currents with different values of the margin angle.

of $\dot{I}_P(n)$ and $\dot{I}_S(n)$ are obtained as

$$\begin{cases} \dot{I}_P(n) = \frac{j(n-1/n)X_S\dot{V}_P(n) - jn\omega M\dot{V}_S(n)}{n^2\omega^2 M^2 - (n-1/n)^2 X_P X_S} \\ \dot{I}_S(n) = \frac{jn\omega M\dot{V}_P(n) - j(n-1/n)X_S\dot{V}_S(n)}{n^2\omega^2 M^2 - (n-1/n)^2 X_P X_S} \end{cases} \tag{34}$$

where

$$\begin{cases} X_P = \omega L_P = 1/\omega C_P \\ X_S = \omega L_S = 1/\omega C_S. \end{cases} \tag{35}$$

Combining (32), (33), and (34), the time-domain expressions of $i_P(t)$ and $i_S(t)$ are derived as

$$\begin{cases} i_P(t) = \sum\limits_{n=0.5,1,1.5,\ldots} I_P(n)\sin(n\omega t + \varphi_P(n)) \\ i_S(t) = \sum\limits_{n=0.5,1,1.5,\ldots} I_S(n)\sin(n\omega t + \varphi_S(n)) \end{cases} \tag{36}$$

where $I_P(n)$ and $\varphi_P(n)$ are the amplitude and phase angle of the nth-order harmonic component of $i_P(t)$; $I_S(n)$ and $\varphi_S(n)$ are the amplitude and phase angle of the nth-order harmonic component of $i_S(t)$, respectively. When the converters operating in the HB mode, the harmonic-considered time-domain expression of $i_P(t)$ and $i_S(t)$ can be deduced in a similar way.

To evaluate the impact of harmonics on the transfer efficiency of the resonant tank, the transfer efficiency error $\Delta\eta$ introduced by neglecting harmonics is expressed as

$$\Delta\eta = (\eta_{fund} - \eta_{har}) \times 100\% \tag{37}$$

where η_{har} denotes the harmonic-considered transfer efficiency; η_{fund} represents the transfer efficiency with only the fundamental component considered. With the parameters listed in Table I, $\Delta\eta$ against U_{out} and P_{out} is depicted in Fig. 13. As shown in Fig. 13, the transfer efficiency error $\Delta\eta$ caused by neglecting harmonics is negligible (less than 0.025%), which means that it is sufficient to analyze the efficiency using fundamental frequency approximation.

Another influence of harmonics is on the ZVS implementation, which is determined by the instantaneous value of the turn-ON current. In order to investigate the impact of harmonics on the ZVS current, i_{ZVS_har} is defined as the minimum ZVS current considering harmonics; i_{ZVS_fund} is defined as the minimum ZVS current with only the fundamental component considered. With the parameters listed in Table I and $U_{out} = 600\,V$, i_{ZVS_fund} and i_{ZVS_har} with different values of the margin angle δ_m are calculated and shown in Fig. 14. As it can be observed from Fig. 14, the minimum ZVS current is reduced due to the harmonics. However, the reduced ZVS current can be compensated by slightly increasing the margin angle δ_m by $2-3°$. Compared with the significant improvement of δ shown in Fig. 9, a small increased value of δ_m is acceptable.

TABLE II
SIMULATED CAPACITOR VOLTAGES AT DIFFERENT POWER POINTS

Mode	Output Power [kW]	V_{CP0} [1] [V]	V_{CPM} [2] [V]	V_{CS0} [1] [V]	V_{CSM} [2] [V]
HB-HB	1.5	300	2351	184	1786
MB-HB	2.2	91	2723	283	2304
MB-MB	3.4	150	3604	93	2722
FB-MB	6.3	0	3759	149	**3440**
FB-FB	10.0	0	**4864**	0	3277

1 DC component of the primary and secondary capacitor voltages.
2 Peak values of the primary and secondary capacitor voltages.
The bold values represent the maximum voltage stress on the primary and secondary capacitors.

F. Capacitor Voltage Stress

When the converter works in the HB and MB modes, the capacitors C_P and C_S need to block a certain dc voltage. With the parameters listed in Table I and $U_{out} = 600\,V$, the simulation results of the capacitor voltages at different power points are presented in Table II. As shown in Table II, the maximum dc blocking voltage of the capacitors occurs at the transition power points between different modes. For the converter working in the HB mode, the ac voltage reaches the full duty cycle at the transition power point, and the dc blocking voltage of the capacitor under this case is $U_{in}/2$ or $U_{out}/2$. For the MB mode, since the converter operates alternately between the FB and HB modes, the maximum dc blocking voltage of the capacitor is $U_{in}/4$ or $U_{out}/4$. Moreover, due to the dc blocking voltage in the hybrid modes, the peak value of the capacitor voltage is increased, and the worst cases are also demonstrated in Table II. For the primary capacitor, the maximum voltage stress occurs at the 10 kW power point in the FB–FB mode, i.e., 4864 V. This means that the introduction of the hybrid modes does not

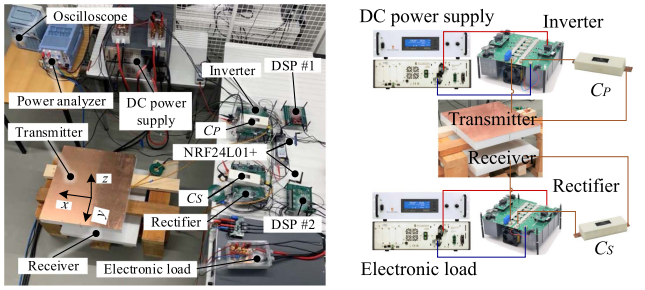

Fig. 15. Experimental prototype of the SS-compensated WPT system. (a) Overall experimental platform. (b) Main circuit of the WPT system.

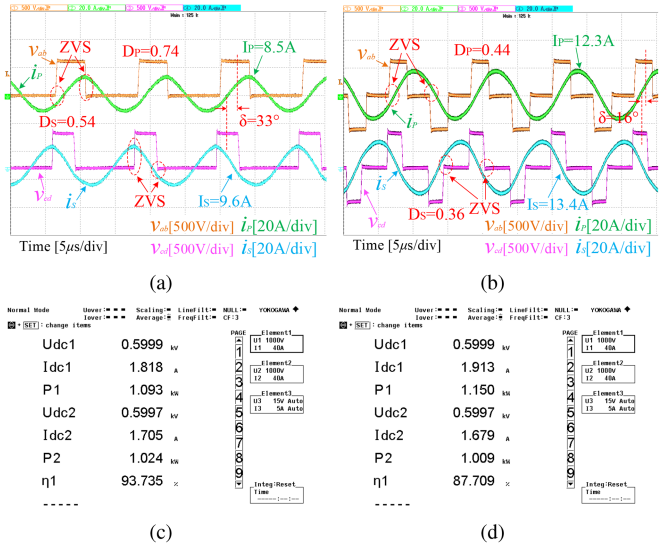

Fig. 16. Steady-state waveforms and efficiency measurement of the HB-HB and FB-FB modes when delivering 1 kW power. (a) Steady-state waveforms of the HB-HB mode. (b) Steady-state waveforms of the FB-FB mode. (c) Efficiency measurement of the HB-HB mode. (d) Efficiency measurement of the FB-FB mode. Herein, $P1$ and $P2$ are the measured input and output powers of the WPT system, respectively, while the notation $\eta 1$ is set as $\eta 1 = P2/P1$ to illustrate the system efficiency.

increase the voltage stress of the primary capacitor. For the secondary capacitor, when the system works in FB–MB mode to deliver 6.3 kW power, the peak value of the secondary capacitor voltage reaches 3440 V due to the influence of dc blocking voltage and subharmonics, which is slightly larger than 3277 V when delivering 10 kW in the FB–FB mode. This means that the voltage stress of the secondary capacitor is increased slightly due to the hybrid modes. However, it is only increased by 5%, which is an acceptable value and can be addressed during the design process.

IV. Experimental Verifications

A. Hardware Setup

To verify the feasibility of the proposed MS-PSC method, an SS-compensated WPT prototype is established, as shown in Fig. 15. A dc source is utilized to provide the required power, with the dc input voltage fixed at 600 V. Another bidirectional dc source, as an electronic load, is connected to the output of the rectifier. In order to measure the dc to dc transfer efficiency, a power analyzer YOKOGAWA WT500 is adopted. The control algorithm and PWM generation are implemented using DSP28379. Three high-voltage parallel-connected SiC MOSFETs IMZ120R030M1H are used as each power switch of the H-bridge converters. The synchronization between the primary and secondary driving signals is realized by the zero-crossing detection technique of the receiver current [9], [26], and the NRF24L01+ module is adopted for the dual-side wireless communication. To ensure ZVS, the margin angle δ_m is set to 16°, and the dead time is configured at 300 ns. More details of the developed system are given in Table I.

B. ZVS Implementation and Efficiency Optimization

To verify the feasibility of the proposed MS-PSC method, experimental results of different operating modes are shown as follows. It should be noted that the dc output voltage U_{out} is regulated to 600 V in these experiments.

When delivering 1 kW power, the steady-state waveforms of the WPT system working in the HB-HB and FB-FB modes are shown in Fig. 16(a) and (b), respectively. As it can be seen, ZVS operations of all power switches are realized in the HB-HB and FB-FB modes. The duty cycles D_P and D_S of the FB-FB mode, as shown in 16(a), are 0.44 and 0.36, respectively. To realize ZVS, the phase angle δ is selected as 16° in the FB-FB mode. Compared with the FB-FB mode, D_P and D_S are increased in the HB-HB mode, and therefore, the value of δ is increased to 33°. As a result, the rms values of the coil currents are reduced in the HB-HB mode, with I_P reduced from 12.3 to 8.5 A, and I_S reduced from 13.4 to 9.6 A, respectively. The measured dc to dc efficiency of these two modes is further presented in Fig. 16(c) and (d). Compared with the FB-FB mode, the dc to dc efficiency of the HB-HB mode is improved from 87.7% to 93.7%.

Experimental results of the MB-HB, MB-MB, and FB-MB modes are also shown in Figs. 17–19, respectively. As it can be observed in Fig. 17, when delivering 2 kW power, δ is increased from 22° to 36° with the operating mode switched from the FB-FB mode to the MB-HB mode. Compared with the FB-FB mode, the efficiency of the MB-HB mode is improved from 90.5% to 94.5%. Similar efficiency optimization can also be observed in the MB-MB and FB-MB modes, with efficiency improvements of 2.4% and 1.8% when delivering 3 and 5 kW power, respectively.

Furthermore, the measured dc to dc transfer efficiency in the power range of 1–10 kW is shown in Fig. 20. Compared with conventional TPS method, the efficiency of the proposed MS-PSC method is greatly improved in the 1–6.3 kW power range, with efficiency improvements ranging from 1.5% to 6%. With the proposed MS-PSC method, the overall efficiency of the system remains between 93.5% to 96.1%. Moreover, the experimental results in terms of the CC and CV output are further presented in Fig. 21 to demonstrate the effectiveness of the proposed MS-PSC method for EV battery charging.

Based on the measured coil currents in the experiments and the simulated FE model in COMSOL, the calculated power loss

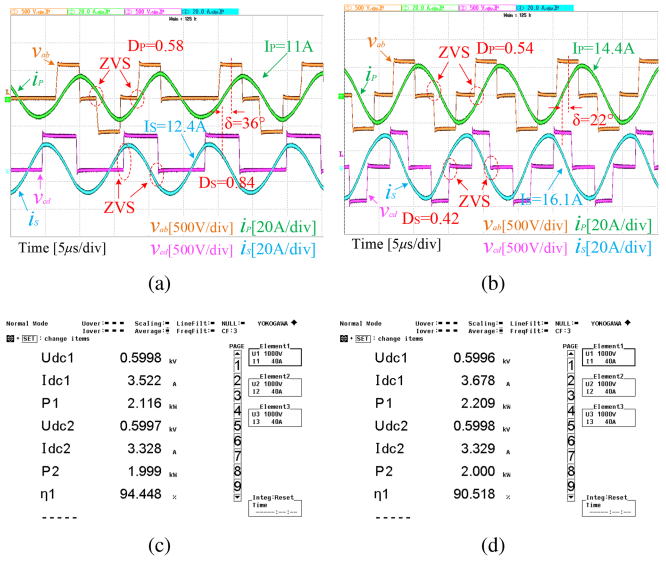

Fig. 17. Steady-state waveforms and efficiency measurement of the MB-HB and FB-FB modes when delivering 2 kW power. (a) Steady-state waveforms of the MB-HB mode. (b) Steady-state waveforms of the FB-FB mode. (c) Efficiency measurement of the MB-HB mode. (d) Efficiency measurement of the FB-FB mode.

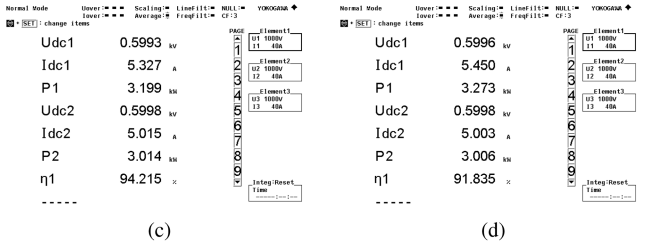

Fig. 18. Steady-state waveforms and efficiency measurement of the MB-MB and FB-FB modes when delivering 3 kW power. (a) Steady-state waveforms of the MB-MB mode. (b) Steady-state waveforms of the FB-FB mode. (c) Efficiency measurement of the MB-MB mode. (d) Efficiency measurement of the FB-FB mode.

distributions of different modes are further presented in Fig. 22. As illustrated in Fig. 22, by using the proposed MS-PSC method, the power losses of each part are significantly reduced. The main reason is that the reactive power is lowered in the MS-PSC method, and smaller coil currents are obtained. Another important reason is that in the HB and MB modes, the equivalent switching times of the power switches are decreased, and thus, the switching loss of the power switches is further reduced.

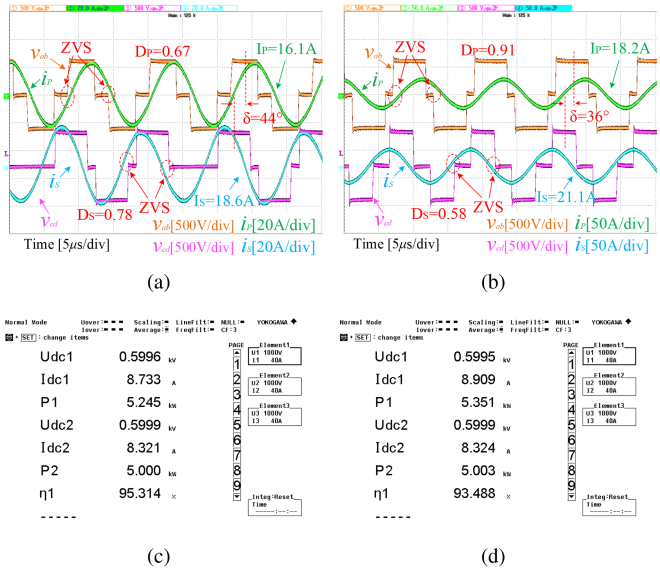

Fig. 19. Steady-state waveforms and efficiency measurement of the FB-MB and FB-FB modes when delivering 5 kW power. (a) Steady-state waveforms of the FB-MB mode. (b) Steady-state waveforms of the FB-FB mode. (c) Efficiency measurement of the FB-MB mode. (d) Efficiency measurement of the FB-FB mode.

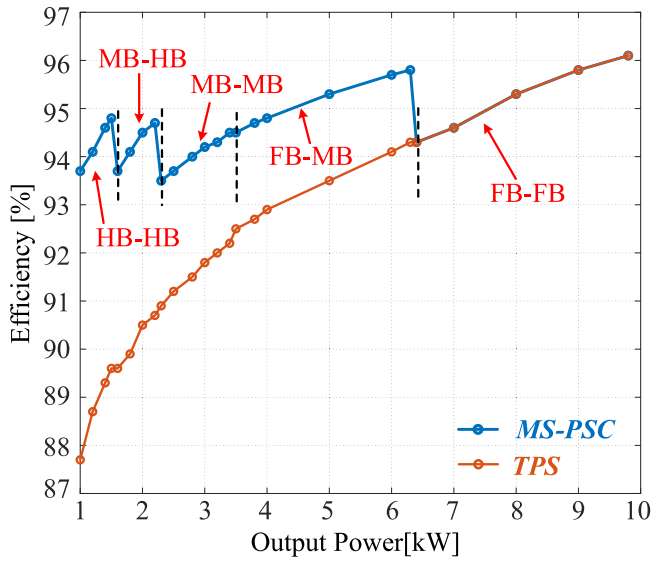

Fig. 20. Measured overall efficiency improvement of the proposed MS-PSC method.

C. Coil Misalignment

The effectiveness of the proposed MS-PSC method is also validated under coil misalignment. The *x*-*y*-*z* direction of the coils is illustrated in Fig. 15(a), and the mutual inductance under *x*-direction misalignment is measured and shown in Fig. 23(a). As it can be observed in Fig. 23(a), the mutual inductance M is decreased from 46 to 35 μH due to the coil misalignment, and therefore, the coupling coefficient is reduced from 0.19 to 0.14. Furthermore, the experiments under 10 cm *x*-direction misalignment are carried out at different power points, and the measured dc to dc efficiency is presented in Fig. 23(b). Compared with the conventional TPS method, the efficiency

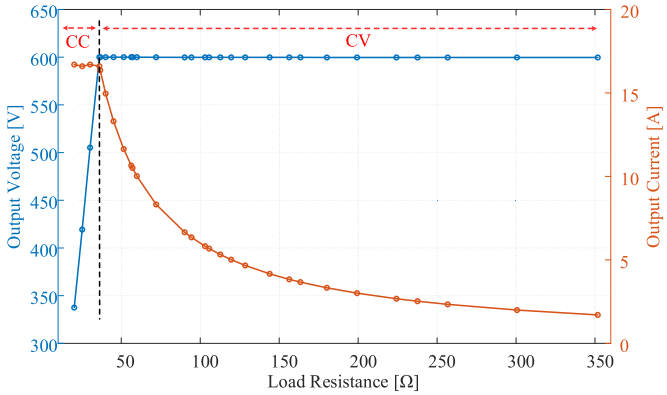

Fig. 21. Experimental results in terms of the CC and CV output of the proposed MS-PSC method.

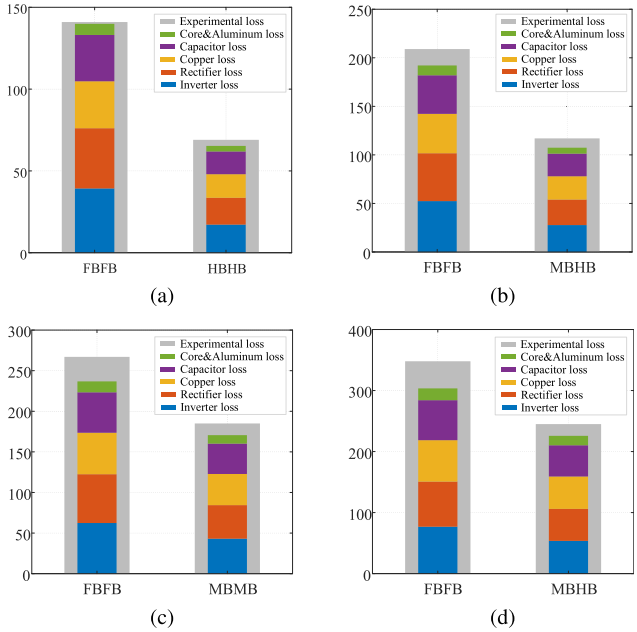

Fig. 22. Calculated power loss distributions in different modes. (a) HB-HB mode and FB-FB mode when delivering 1 kW power. (b) MB-HB mode and FB-FB mode when delivering 2 kW power. (c) MB-MB mode and FB-FB mode when delivering 3 kW power. (d) FB-MB mode and FB-FB mode when delivering 5 kW power. Herein, the calculated total loss is compared with the experimental results, with the maximum relative error at 12.8%.

of the proposed MS-PSC method is improved in the 1–8.3 kW power range, with the efficiency improvements ranging from 1.5% to 7.5%. As a result, the overall efficiency of the system remains between 91.7% to 95.2%. Moreover, comparing Figs. 20 and 23 reveals that the transition power points between different modes are varied due to the coupling changes. Hence, in practical applications, when the system needs to deal with the coil misalignment, it is recommended to establish a lookup table based on different mutual inductance values. Although this introduces small errors due to inevitable parameter shifts and measurement errors, it is acceptable as the mode switching

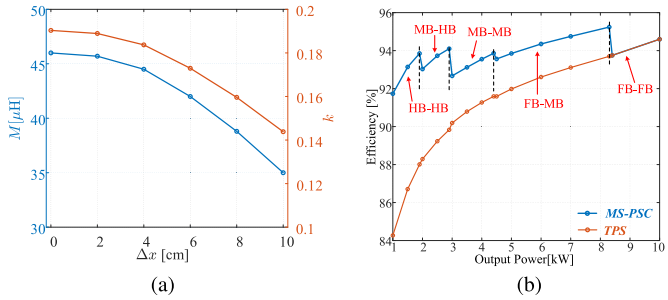

Fig. 23. Performance of the proposed MS-PSC method under coil misalignment. (a) Variations in mutual inductance and coupling coefficient. (b) Measured dc–dc efficiency under 10 cm x-direction coil misalignment.

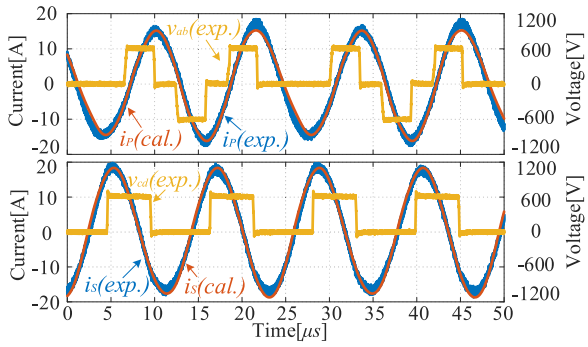

Fig. 24. Experimental and calculated waveforms when delivering 2 kW power in the MB-HB mode.

is only for efficiency optimization and very precise transition power points are not required.

D. Accuracy of the Harmonic-Considered Model

To verify the accuracy of the harmonic-considered model described in Section III-E, experimental and calculated results of the MB-HB mode when delivering 2 kW power are presented as an example in Fig. 24. As it can be seen, the calculated current waveforms based on the harmonic-considered model basically coincide with the experimental current waveforms. This indicates that the harmonic-considered model is accurate enough for analyzing the influence of harmonics. Furthermore, the experimental and calculated minimum ZVS current I_{min_ZVS} are also compared in Fig. 25. As illustrated in Fig. 25, the experimental results of I_{min_ZVS} are close to that of the calculated results, and ZVS can be guaranteed under the full power range.

E. Dynamic Response

To evaluate the dynamic performance of the proposed MS-PSC method, transient response experiments are carried out under different loads and reference voltages. In these experiments, the dc output voltage is tracked through PI control as described in Fig. 10, and the mode transition power points are calculated based on the proposed mode selection strategy. In Fig. 26(a), the reference output voltage is set to 600 V, with the load changed from 250 to 200 Ω. As it can be seen, the operating mode changes

TABLE III
COMPARISON WITH OTHER REPORTED CONTROL METHODS

Reference	Method	Coupling coefficient	No extra circuits	Rated power P_R	Efficiency optimization range	Efficiency
[17]	DPS	0.217	Yes	1 kW	10%–100% P_R	80%–93%
[18]	TPS	0.14–0.2	Yes	1 kW	16%–100% P_R	90%–94.83%
[19]	SCC-PSM	0.15–0.2	No	500 W	20%–100% P_R	83%–94.7%
[20]	VFPSC	0.22	Yes	2.2 kW	12.5%–100% P_R	91%–96.4%
[23]	HMC	0.383	Yes	1.8 kW	16.7%–100% P_R	92.49%–94.29%
[24]	DSC-MS	0.15–0.23	Yes	270 W	14.8%–100% P_R	88.07%–93.9%
This article	MS-PSC	0.19	Yes	10 kW	10%–100% P_R	93.5%–96.1%

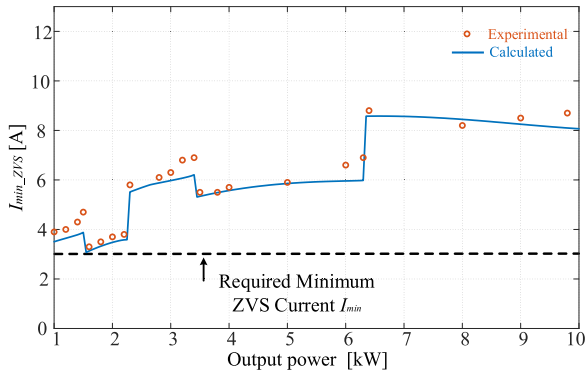

Fig. 25. Comparison of the experimental and calculated minimum ZVS current I_{min_ZVS}. Herein, the required minimum ZVS current I_{min} is calculated as 3 A based on the analysis in [21].

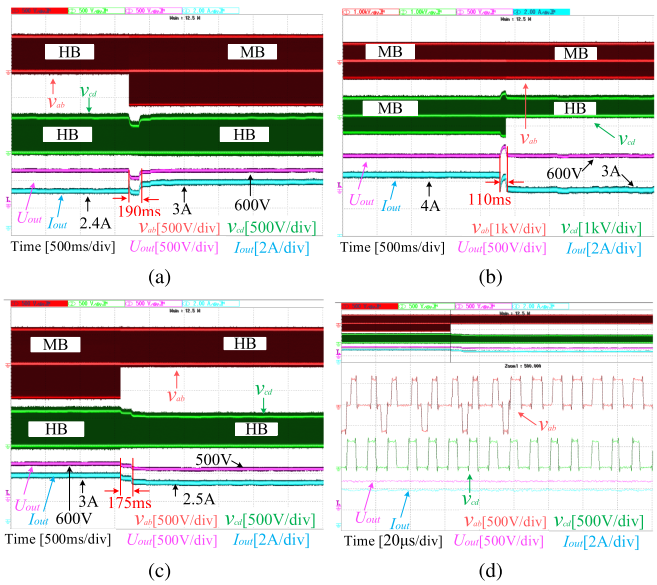

Fig. 26. Dynamic performance of the proposed MS-PSC method. (a) When the load changes from 250 Ω to 200 Ω. (b) When the load changes from 150 to 200 Ω. (c) When the reference output voltage changes from 600 to 500 V. (d) Enlarged view of Fig. 26(c).

from the HB-HB mode to the MB-HB mode when the output power is increased from 1.44 to 1.8 kW. The dc output voltage is tightly controlled to the reference value, with the dynamic setting time at 190 ms. The dynamic performance of the system with the load changed from 150 to 200 Ω is further presented in Fig. 26(b). As it can be observed, the system switches from the MB-MB mode to the MB-HB mode when the output power is decreased from 2.4 to 1.8 kW, with the setting time at 110 ms. In Fig. 26(c), the reference output voltage is suddenly changed from 600 to 500 V with the load fixed at 200 Ω. The experiment shows that with the proposed MS-PSC method, the system can track the reference output voltage accurately in a response time of 175 ms. An enlarged view of Fig. 26(c) during the mode transition moment is then presented in Fig. 26(d), which shows that the MS-PSC method can realize mode switching seamlessly.

F. Comparison With Previous Control Strategies

In recent years, many control methods have been proposed to achieve wide ZVS operations and efficiency optimization. In order to demonstrate the difference between the proposed MS-PSC method and other reported control strategies, detailed performance comparisons are summarized in Table III.

Compared to other reported literatures, the main contribution of this article is to combine FB, MB, and HB modes together and apply them in both the inverter and the rectifier. As a result, ZVS operations are realized with minimized reactive power, and efficiency optimization is achieved in a wide power range. The proposed MS-PSC method in this article can achieve an overall efficiency of 93.5%–96.1% in the range of 10%–100% of the rated power, with the coupling coefficient $k = 0.19$.

V. CONCLUSION

In this article, an MS-PSC method is proposed for ZVS implementation and efficiency optimization in a wide power range. Power regulation, load matching, and wide ZVS operations are realized without using any auxiliary circuits. Moreover, thanks to the effective use of FB, MB, and HB modes as well as the cooperative operation of the inverter and rectifier, this method can realize wide ZVS operations with minimized reactive power. Compared with conventional TPS control, smaller coil currents are obtained in the MS-PSC method when delivering the same amount of power. As a result, the overall efficiency of the system is enhanced significantly. Experimental results show that the proposed MS-PSC method can realize an overall efficiency of 93.5%–96.1% in the power range of 1–10 kW.

REFERENCES

[1] A. A. Mohamed, A. A. Shaier, H. Metwally, and S. I. Selem, "A comprehensive overview of inductive pad in electric vehicles stationary charging," *Appl. Energy*, vol. 262, 2020, Art. no. 114584.

[2] Z. Zhang, H. Pang, A. Georgiadis, and C. Cecati, "Wireless power transfer–An overview," *IEEE Trans. Ind. Electron.*, vol. 66, no. 2, pp. 1044–1058, Feb. 2019.

[3] W. V. Wang, D. J. Thrimawithana, and M. Neuburger, "An Si MOSFET-based high-power wireless EV charger with a wide ZVS operating range," *IEEE Trans. Power Electron.*, vol. 36, no. 10, pp. 11163–11173, Oct. 2021.

[4] A. Ahmad, M. S. Alam, and R. Chabaan, "A comprehensive review of wireless charging technologies for electric vehicles," *IEEE Trans. Transp. Electrific.*, vol. 4, no. 1, pp. 38–63, Mar. 2018.

[5] P. Machura and Q. Li, "A critical review on wireless charging for electric vehicles," *Renewable Sustain. Energy Rev.*, vol. 104, pp. 209–234, 2019.

[6] W. Shi et al., "Design of a highly efficient 20 kW inductive power transfer system with improved misalignment performance," *IEEE Trans. Transport. Electrific.*, vol. 8, no. 2, pp. 2384–2399, Jun. 2022.

[7] M. Kim, D.-M. Joo, and B. K. Lee, "Design and control of inductive power transfer system for electric vehicles considering wide variation of output voltage and coupling coefficient," *IEEE Trans. Power Electron.*, vol. 34, no. 2, pp. 1197–1208, Feb. 2019.

[8] A. C. Bagchi, A. Kamineni, R. A. Zane, and R. Carlson, "Review and comparative analysis of topologies and control methods in dynamic wireless charging of electric vehicles," *IEEE Trans. Emerg. Sel. Topics Power Electron.*, vol. 9, no. 4, pp. 4947–4962, Aug. 2021.

[9] Y. Jiang, L. Wang, Y. Wang, J. Liu, X. Li, and G. Ning, "Analysis, design, and implementation of accurate ZVS angle control for EV battery charging in wireless high-power transfer," *IEEE Trans. Ind. Electron.*, vol. 66, no. 5, pp. 4075–4085, May 2019.

[10] M. Fu, H. Yin, X. Zhu, and C. Ma, "Analysis and tracking of optimal load in wireless power transfer systems," *IEEE Trans. Power Electron.*, vol. 30, no. 7, pp. 3952–3963, Jul. 2015.

[11] T. Zhang, M. Fu, C. Ma, and X. Zhu, "Optimal load analysis for a two-receiver wireless power transfer system," in *Proc. IEEE Wireless Power Transfer Conf.*, 2014, pp. 84–87.

[12] X. Dai, X. Li, Y. Li, and A. P. Hu, "Maximum efficiency tracking for wireless power transfer systems with dynamic coupling coefficient estimation," *IEEE Trans. Power Electron.*, vol. 33, no. 6, pp. 5005–5015, Jun. 2018.

[13] Z. Huang, S.-C. Wong, and K. T. Chi, "Control design for optimizing efficiency in inductive power transfer systems," *IEEE Trans. Power Electron.*, vol. 33, no. 5, pp. 4523–4534, May 2018.

[14] W. Zhong and S. Hui, "Maximum energy efficiency tracking for wireless power transfer systems," *IEEE Trans. Power Electron.*, vol. 30, no. 7, pp. 4025–4034, Jul. 2015.

[15] T. Diekhans and R. W. De Doncker, "A dual-side controlled inductive power transfer system optimized for large coupling factor variations and partial load," *IEEE Trans. Power Electron.*, vol. 30, no. 11, pp. 6320–6328, Nov. 2015.

[16] R. Mai, Y. Liu, Y. Li, P. Yue, G. Cao, and Z. He, "An active-rectifier-based maximum efficiency tracking method using an additional measurement coil for wireless power transfer," *IEEE Trans. Power Electron.*, vol. 33, no. 1, pp. 716–728, Jan. 2018.

[17] Y. Li, J. Hu, F. Chen, Z. Li, Z. He, and R. Mai, "Dual-phase-shift control scheme with current-stress and efficiency optimization for wireless power transfer systems," *IEEE Trans. Circuits Syst. I: Regular Papers*, vol. 65, no. 9, pp. 3110–3121, Sep. 2018.

[18] X. Zhang et al., "A control strategy for efficiency optimization and wide ZVS operation range in bidirectional inductive power transfer system," *IEEE Trans. Ind. Electron.*, vol. 66, no. 8, pp. 5958–5969, Aug. 2019.

[19] X. Wang, J. Xu, M. Leng, H. Ma, and S. He, "A hybrid control strategy of LCC-S compensated WPT system for wide output voltage and ZVS range with minimized reactive current," *IEEE Trans. Ind. Electron.*, vol. 68, no. 9, pp. 7908–7920, Sep. 2021.

[20] H. Hu, T. Cai, S. Duan, X. Zhang, J. Niu, and H. Feng, "An optimal variable frequency phase shift control strategy for ZVS operation within wide power range in IPT systems," *IEEE Trans. Power Electron.*, vol. 35, no. 5, pp. 5517–5530, May 2020.

[21] H. Li, J. Fang, S. Chen, K. Wang, and Y. Tang, "Pulse density modulation for maximum efficiency point tracking of wireless power transfer systems," *IEEE Trans. Power Electron.*, vol. 33, no. 6, pp. 5492–5501, Jun. 2018.

[22] W. Zhong and S. Hui, "Maximum energy efficiency operation of series-series resonant wireless power transfer systems using on-off keying modulation," *IEEE Trans. Power Electron.*, vol. 33, no. 4, pp. 3595–3603, Apr. 2018.

[23] Y. Li, W. Sun, X. Zhu, and J. Hu, "A hybrid modulation control for wireless power transfer systems to improve efficiency under light-load conditions," *IEEE Trans. Ind. Electron.*, vol. 69, no. 7, pp. 6870–6880, Jul. 2022.

[24] M. Wu et al., "A dual-sided control strategy based on mode switching for efficiency optimization in wireless power transfer system," *IEEE Trans. Power Electron.*, vol. 36, no. 8, pp. 8835–8848, Aug. 2021.

[25] B. X. Nguyen et al., "An efficiency optimization scheme for bidirectional inductive power transfer systems," *IEEE Trans. Power Electron.*, vol. 30, no. 11, pp. 6310–6319, Nov. 2015.

[26] Y. Jiang et al., "Phase-locked loop combined with chained trigger mode used for impedance matching in wireless high power transfer," *IEEE Trans. Power Electron.*, vol. 35, no. 4, pp. 4272–4285, Apr. 2020.

Gangwei Zhu (Student Member, IEEE) was born in Hunan, China, in 1997. He received the B.S. degree from Central South University, Changsha, China, in 2018, and the M.S. degree from Shanghai Jiao Tong University, Shanghai, China, in 2021, both in electrical engineering. He is currently working toward the Ph.D. degree in electrical engineering with the Delft University of Technology, Delft, The Netherlands.

His research interests include advanced control and modulation for wireless power transfer.

Jianning Dong (Senior Member, IEEE) received the B.S. and Ph.D. degrees in electrical engineering from Southeast University, Nanjing, China, in 2010 and 2015, respectively.

He was a Postdoctoral Researcher with the McMaster Automotive Resource Centre, McMaster University, Hamilton, ON, Canada. Since 2016, he has been an Assistant Professor with the DC System, Energy Conversion and Storage (DCE&S) Group, Delft University of Technology (TU Delft), Delft, The Netherlands. His research interests include electromechanical energy conversion and contactless power transfer.

Wenli Shi (Student Member, IEEE) received the B.S. degree in automotive engineering from Jilin University, Changchun, China, in 2015, and the M.S. degree in mechanical engineering from the Beijing Institute of Technology, China, in 2018. He is currently working toward the Ph.D. degree in dynamic wireless charging of electric vehicles with the DC System, Energy Conversion and Storage (DCE&S) Group, Delft University of Technology (TU Delft), Delft, The Netherlands.

His research interests include foreign object detection, multiobjectives optimization design, dynamic modeling, and control for wireless power transfer.

Thiago Batista Soeiro (Senior Member, IEEE) received the B.Sc. (Hons.) and M.Sc. degrees in electrical engineering from the Federal University of Santa Catarina, Florianopolis, Brazil, in 2004 and 2007, respectively, and the Ph.D. degree in electrical engineering from the Swiss Federal Institute of Technology, Zurich, Switzerland, in 2012.

During the Master and Ph.D. studies, he was a Visiting Scholar with the Power Electronics and Energy Research Group, Concordia University, Montreal, QC, Canada, and with the Center for Power Electronics Systems, Blacksburg, VA, USA, respectively. From 2012 to 2013, he was a Researcher with the Power Electronics Institute, Federal University of Santa Catarina. From October 2013 to April 2018, he worked with the Corporate Research Center, ABB Switzerland Ltd., Baden-Dattwil, Switzerland, where he was a Senior Scientist. From May 2018 to January 2022, he worked with the DC Systems, Energy Conversion and Storage Group, Delft University of Technology, Delft, The Netherlands, where he was an Associate Professor. From January to October 2022, he worked with the Power Management and Distribution Section (TEC-EPM) for the European Space Research and Technology Centre, Noordwijk, the Netherlands. In October 2022, he became a Full Professor for Power Electronics with the Power Electronics and EMC Group, University of Twente, Enschede, The Netherlands. His research interests include advanced high power converters and dc system integration.

Dr. Soeiro was the recipient of the 2013 IEEE Industrial Electronics Society Best Conference Paper Award and the Best Paper Awards in the following IEEE conferences: International Conference on Power Electronics (ECCE Asia 2011), the International Conference on Industrial Technology (ICIT 2013), the Conference on Power Electronics and Applications EPE2015 (ECCE Europe 2015), and the International Conference on Power Electronics and Motion Control 2020 and 2022 (PEMC 2020 and 2022).

Junzhong Xu (Member, IEEE) was born in Ningbo, China, in 1994. He received the B.S. degree from the Harbin Institute of Technology, Harbin, China, in 2016, and the Ph.D. degree from Shanghai Jiao Tong University, Shanghai, China, in 2021, both in electrical engineering.

From 2020 to 2021, he was a Visiting Scholar with the DC Systems, Energy Conversion and Storage Group, Delft University of Technology, Delft, The Netherlands. He worked as a Postdoctoral Research Fellow with the Department of Electrical Engineering, Shanghai Jiao Tong University, Shanghai, China, in 2021. He is currently with Power Electronic Systems (PES) Laboratory, the Swiss Federal Institute of Technology (ETH), Zurich, Switzerland. His research interests include advanced control and modulation for power converters.

Dr. Xu was the recipient of the Outstanding Ph.D. Thesis Award from Shanghai Jiao Tong University in 2021.

Pavol Bauer (Senior Member, IEEE) received the master's degree in electrical engineering from the Technical University of Kosice, Kosice, Slovakia, in 1985, and the Ph.D. degree in electrical engineering from the Delft University of Technology, Delft, The Netherlands, in 1995.

From 2002 to 2003, he was with KEMA (DNV GL), Arnhem, The Netherlands, on different projects related to power electronics applications in power systems. He is currently a Full Professor with the Department of Electrical Sustainable Energy, Delft University of Technology, and the Head of DC Systems, Energy Conversion, and Storage Group. He is also a Professor with the Brno University of Technology, Brno, Czech Republic, and an Honorary Professor with the Politehnica University Timisoara, Timisoara, Romania. He has authored or coauthored over 120 journal articles and 500 conference papers in his field. He is an author or coauthor of eight books, holds seven international patents, and organized several tutorials at international conferences. He has worked on many projects for the industry concerning wind and wave energy, power electronic applications for power systems such as Smarttrafo; HVdc systems, projects for smart cities such as photovoltaic (PV) charging of electric vehicles, PV and storage integration, contactless charging; and he participated in several Leonardo da Vinci and H2020, and Electric Mobility Europe EU projects as a Project Partner (ELINA, INETELE, E-Pragmatic, Micact, Trolley 2.0, OSCD, P2P, and Progressus) and a Coordinator (PEMCWebLab.com-Edipe, SustEner, Eranet DCMICRO).

Dr. Bauer is the Former Chairman of Benelux IEEE Joint Industry Applications Society, Power Electronics and Power Engineering Society Chapter, the Chairman of the Power Electronics and Motion Control Council, a Member of the Executive Committee of European Power Electronics Association, and also a Member of the International Steering Committee at numerous conferences.